J. Fluid Mech. (2025), *vol.* 1017, R1, doi:10.1017/jfm.2025.10458

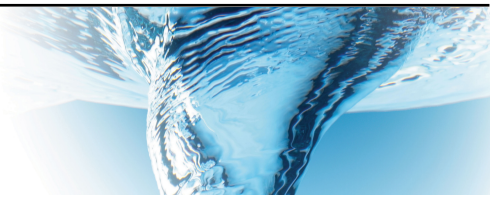

Jamming of elastoviscoplastic fluids in elastic turbulence

Christopher Soriano From[1], **Vedad Dzanic**[2], **Vahid Niasar**[1] **and Emilie Sauret**[2]

[1]Department of Chemical Engineering, University of Manchester, Manchester M13 9PL, UK

[2]School of Mechanical, Medical and Process Engineering, Faculty of Engineering, Queensland University of Technology, Brisbane, QLD 4001, Australia

Corresponding authors: Christopher Soriano From, christopher.from@manchester.ac.uk; Vedad Dzanic, v2.dzanic@qut.edu.au

(Received 2 March 2025; revised 23 May 2025; accepted 1 July 2025)

Elastoviscoplastic (EVP) fluid flows are driven by a non-trivial interplay between the elastic, viscous and plastic properties, which under certain conditions can transition the otherwise laminar flow into complex flow instabilities with rich space–time-dependent dynamics. We discover that under elastic turbulence regimes, EVP fluids undergo dynamic jamming triggered by localised polymer stress deformations that facilitate the formation of solid regions trapped in local low-stress energy wells. The solid volume fraction ϕ, below the jamming transition $\phi < \phi_J$, scales with $\sqrt{Bi}$, where Bi is the Bingham number characterising the ratio of yield to viscous stresses, in direct agreement with theoretical approximations based on the laminar solution. The onset of this new dynamic jamming transition $\phi \geqslant \phi_J$ is marked by a clear deviation from the scaling $\phi \sim \sqrt{Bi}$, scaling as $\phi \sim \exp Bi$. We show that this instability-induced jamming transition – analogous to that in dense suspensions – leads to slow, minimally diffusive and rigid-like flows with finite deformability, highlighting a novel phase change in elastic turbulence regimes of complex fluids.

Key words: viscoelasticity, plastic materials, shear-flow instability

1. Introduction

Complex non-Newtonian fluids are well-known to be subject to unpredictable flow instabilities (Steinberg 2021; Datta *et al.* 2022), a problem whose motivations originated from industry over 60 years ago due to production quality issues in processing operations

involving polymeric fluids (Petrie & Denn 1976), which has continued to intrigue the scientific and industrial communities since (Dubief, Terrapon & Hof 2023). In particular, elastoviscoplastic fluids (EVP) characterised by their ability to exhibit elastic, viscous and plastic behaviours depending on applied stress are ubiquitous in various processes in nature (such as lava and landslide flow (Jerolmack & Daniels 2019; Abdelgawad, Cannon & Rosti 2023) and certain biological substances (Bertsch *et al.* 2022)) and industry, including materials such as pastes and gels (Balmforth, Frigaard & Ovarlez 2014; Nicolas *et al.* 2018). The EVP materials, a class of non-Newtonian 'yield stress' fluids, behave as elastic solids with finite deformations below their yield criteria and above which flow like complex viscoelastic fluids (Bonn *et al.* 2017; Nicolas *et al.* 2018). Understanding the dynamics of EVP fluid flows remains an essential area of research that bridges fundamental science and practical applications. A fascinating and challenging aspect of EVP fluid flows is the occurrence of instabilities driven by a delicate balance between this solid-like and liquid-like behaviour that is highly localised and time-dependent (Nicolas *et al.* 2018; Varchanis *et al.* 2020). Flow instabilities in EVP fluids are prominent when subjected to deformation rates near their material yield stress, making their applications unpredictable and difficult to control (Balmforth *et al.* 2014; Nicolas *et al.* 2018). Insights into these pave the way for innovations in material design and process optimisation, addressing challenges across a wide range of industries and disciplines, from the production of fast-moving consumer goods (Balmforth *et al.* 2014; Bonn *et al.* 2017) to emerging technologies, such as three-dimensional (3-D) printing soft biomaterials (Bertsch *et al.* 2022; Smith & Hashmi 2024; Zhang, Dolatshahi-Pirouz & Orive 2024).

Unlike inertial instabilities that arise in Newtonian fluid flows, such as turbulent flows, viscoelastic fluid flow instabilities arise even without inertial effects in the low-Reynolds-number regime $Re = \rho V \ell/\mu \leqslant 1$ (Groisman & Steinberg 2000). Inertialess instabilities can manifest in various forms (Datta *et al.* 2022), including shear banding (Cochran *et al.* 2024), where regions of differing shear rates develop, and elastic instabilities, where the fluid's elastic nature leads to flow irregularities. The viscous to elastic effects are measured by the Weissenberg number $Wi = \lambda V/\ell \gg 1$, and the viscoelastic to inertial effects are characterised by the elasticity number $El \equiv Wi/Re = \lambda\mu/(\rho\ell^2) \gg 1$. Here, λ is the longest polymer relaxation time, the characteristic length scale is ℓ, ρ is density, μ is total viscosity, and the characteristic velocity is V. The additional property, a yield stress criteria σ_y, traditionally referred to as a jamming transition in EVP material (i.e. the transition from a jammed solid state to a fluid-like state) (Bonn *et al.* 2017), and its ratio to the viscous stress is characterised by the Bingham number $Bi = \sigma_y \ell/(\mu V)$. Time-dependent EVP flows often lead to non-homogeneity with complex flow patterns and transitions (Abdelgawad *et al.* 2023; Dzanic, From & Sauret 2024). More specifically, the elastic property generates an anisotropic stress contribution, which, in extreme cases (i.e. $Re \leqslant 1$), can transition the flow to a chaotic self-sustaining state, known as elastic turbulence (ET), initially discovered to be triggered by linear hoop stress instabilities in curvilinear geometries (Groisman & Steinberg 2000; Steinberg 2021). Later studies identified ET in rectilinear geometries – such as, notably, in viscoelastic Kolmogorov flow by Boffetta *et al.* (2005*b*) – have recently been shown to be triggered by the mechanism known as a centre-mode instability (Kerswell & Page 2024; Lewy & Kerswell 2025), giving rise to 'arrowhead' structures (Page, Dubief & Kerswell 2020) that interact chaotically, transitioning the flow to ET through a bursting scenario. Plasticity on its own (i.e. viscoplasticity where there is negligible elasticity) can dramatically impact fluid flows. Notably, recent work (Abdelgawad *et al.* 2023) demonstrated that plasticity $Bi > 1$ significantly alters both the energy distribution and intermittency of inertial turbulence $Re \gg 10^3$, altering Kolmogorov's well-known inertial and dissipative 5/3

scaling exponent to a new scaling exponent of 2.3. On the other hand, the study of instabilities in inertialess EVP fluid flows, combining both elastic and plastic behaviours, is limited. Our recent work on EVP extensional flows in the ET regime (Dzanic *et al.* 2024) illustrated that the regions of unyielded material increase – indicated by a higher solid volume fraction (ϕ) – as Bi increases. We found that the impact of plasticity on the dynamic behaviour, including transitions to periodic, aperiodic and chaotic regimes, is highly dependent on the flow geometry.

In this work, we discover that EVP fluid flows transition to a jammed state with Bi. The connection to jamming has not previously been made for EVP fluid flows. This elastic-plastic-induced jamming phenomenon is notably distinct from the traditional intuition of jamming transitions in EVP fluids defined as the material's yield stress criterion σ_y (Nicolas *et al.* 2018; N'Gouamba *et al.* 2019). To gain a better understanding of the nature and impact of this phase transition, we demonstrate the direct analogue features of jamming in inertialess EVP flows in the ET regime. We show that intermediate ϕ-regimes approaching jamming from below $\phi \to \phi_J$ follow a square-root scaling behaviour $\phi \sim \sqrt{Bi}$, reminiscent of scaling behaviour in dense suspensions. Beyond the jamming transition $\phi > \phi_J$, the scaling behaviour transitions dramatically – a key signature of a phase transition – growing exponentially as $\phi \sim \exp Bi$.

2. Methods

We numerically study inertialess EVP instabilities with the well-known Kolmogorov flow problem in a two-dimensional (2-D) domain $\boldsymbol{x}$ with double periodic boundary conditions. The dimensionless governing equations of the EVP fluid are given by the incompressible Navier–Stokes equation,

$$\nabla \cdot \boldsymbol{u} = 0, \quad Re\frac{\mathrm{D}\boldsymbol{u}}{\mathrm{D}t} = -\nabla P + \beta \boldsymbol{\Delta u} + \nabla \cdot \boldsymbol{\sigma} + \boldsymbol{F}_0, \tag{2.1}$$

coupled with the polymer stress tensor, $\boldsymbol{\sigma} = Wi^{-1}(1-\beta)(f\boldsymbol{C} - \boldsymbol{I})$, described by a space–time dependent conformation tensor ($\boldsymbol{C}$) constitutive equation,

$$\frac{\mathrm{D}\boldsymbol{C}}{\mathrm{D}t} = \boldsymbol{C} \cdot (\nabla \boldsymbol{u}) + (\nabla \boldsymbol{u})^{\mathsf{T}} \cdot \boldsymbol{C} - \frac{\mathcal{F}}{Wi}(f\boldsymbol{C} - \boldsymbol{I}) + \kappa \boldsymbol{\Delta C}. \tag{2.2}$$

The functions $f = (L^2 - \mathrm{tr}\,\boldsymbol{I})/(L^2 - \mathrm{tr}\boldsymbol{C})$ and $\mathcal{F}(\sigma_v, Bi) = \max(0, (\sigma_v - Bi)/\sigma_v)$ are constitutive polymer models, namely the finite extensible nonlinear elastic Peterlin (FENE-P) model (Peterlin 1961) and the Saramito yield stress model (Saramito 2007), for the elastic and plastic non-Newtonian behaviour, respectively. The yield stress is defined by $\sigma_v = \sqrt{\sigma_{J2}}$ (Saramito 2007), where $\sigma_{J2} = (1/2)(\boldsymbol{\sigma}_d : \boldsymbol{\sigma}_d)$ is the second invariant of the deviatoric part of the stress tensor $\boldsymbol{\sigma}_d = \boldsymbol{\sigma} - \boldsymbol{I}(\mathrm{tr}\,\boldsymbol{\sigma}/\mathrm{tr}\,\boldsymbol{I})$. The model predicts recoverable Kelvin–Voigt viscoelastic deformation in the unyielded state ($\mathcal{F} = 0$ for $\sigma_v \leqslant Bi$), whereas the FENE-P viscoelastic model is retained beyond yielding ($0 \lesneqq \mathcal{F} \leqslant 1$ for $\sigma_v > Bi$), and in the purely viscoelastic limit $Bi = 0 \Rightarrow \mathcal{F} = 1$. Here, L is the maximum polymer extensibility ($L^2 > \mathrm{tr}\boldsymbol{C}$), which we set to $L = 50$, characteristic polymer concentration $\beta = \nu_s/(\nu_s + \nu_p) = 0.9$ as in Rosti *et al.* (2018); Abdelgawad *et al.* (2023), ν_s and ν_p are the solvent and polymer viscosity, respectively, $\boldsymbol{I}$ is the identity tensor ($\mathrm{tr}\,\boldsymbol{I} = 2$), $\boldsymbol{u}$ is the velocity field, P the pressure, and $\boldsymbol{F}_0$ is the external driving force (total force $\boldsymbol{F} = \boldsymbol{F}_p + \boldsymbol{F}_0$, where $\boldsymbol{F}_p = \nabla \cdot \boldsymbol{\sigma}$). Equations (2.1) and (2.2) are solved using a symmetric positive-definite conserving numerical solver developed in-house (Dzanic *et al.* 2024, 2022*a*,*b*,*c*,*d*), comprising the lattice Boltzmann method coupled with a high-order finite-difference scheme. Let $\boldsymbol{n}$ be the level of

periodicity in each direction, where setting $n_x, n_y > 1$ results in $n_x \times n_y$ unit cells. For all simulations, we set $n_x = 6$ and $n_y = 4$, ensuring unicity is conserved, with $N^2 = 128^2$ grid points in each unit cell, i.e. spatial resolution of $2\pi/N$ (we present grid convergence test in the supplementary material, § S1.3, figures S1 and S2). Numerical regularity is added to (2.2) through an additional term $\kappa \boldsymbol{\Delta C}$ with a specified artificial diffusivity κ. While this numerical regularity strategy remains highly debated (Dzanic *et al.* 2022*b*; Couchman *et al.* 2024; Yerasi *et al.* 2024), it is essential to simulate ET flow regimes due to inherent steep polymer stress gradients (Dzanic *et al.* 2022*c*; Gupta & Vincenzi 2019). We minimise κ and any associated artefacts by setting the admissible Schmidt number $Sc = \nu_s/\kappa = 10^3$ as in Berti *et al.* (2008), resulting in $\kappa = 1.6 \times 10^{-4}$, which is smaller than that in recent work (Nichols, Guy & Thomases 2025), an order of magnitude of those realistically expected from the diffusion of the polymer's centre of mass in kinetic theory (Morozov 2022). Full details on the employed methodology are reported in the supplementary material, § S1.

The Kolmogorov shear flow is driven by a constant external force $\boldsymbol{F}_0 = (F_x, F_y)$, given by $F_x(y) = F_0 \cos(Ky)$, $F_y = 0$, with an amplitude $F_0 = V\nu K^2$, scaled with the characteristic peak laminar velocity V in the absence of polymer stress diffusion ($\kappa = 0$) imposing a constant pressure gradient $\partial_x P = F_0 \cos(Ky)$, where $K = 2$ is the spatial frequency $\ell = 1/K$ and the turnover time $T = \nu_s K/F_0$. (Note, the base laminar flow, $\max_y(u_x(y))$, is approximately V; however, the deviation is negligible with the small but finite diffusivity $\kappa = \mathcal{O}(10^{-4})$ since $\max_y(u_x(y)) \to V$ in the limit $\kappa \to 0$.) The flow is in the inertialess ET regime, and, as such, we set $Re = 1$ and $Wi = 20$, such that elastic effects are dominant over inertial effects $El = 20$. In doing so, we limit all the observed changes to the well-known viscoelastic Kolmogorov flow (Boffetta *et al.* 2005*b*; Berti *et al.* 2008; Berti & Boffetta 2010; Kerswell & Page 2024; Lewy & Kerswell 2025) to be due to the introduction of plasticity, which we vary by Bi.

3. Results

When dealing with EVP fluids in practice, a macroscopic point of view of the yield transition is usually adopted, where it is assumed that an applied shear above the yield criteria σ_y will sufficiently shear-thin the material, allowing it to flow (Dennin 2008; Bonn *et al.* 2017). Here, we will model directly how much of the domain remains solid (unyielded) under the imposed flow field. The solid volume fraction is calculated by $\phi(t) = \mathcal{V}_{\mathcal{F}=0}(t)/\mathcal{V} = |\{k : \mathcal{F}(x_k, t) = 0\}|/(n_x n_y N^2)$ where ':' denotes the set formed by the unyielded regions ($\mathcal{F} = 0$) of k, and '$|\cdot|$' denotes cardinality (Dzanic *et al.* 2024). The polymer stretching tr $\boldsymbol{C}$ field at various Bi is shown in figure 1. (See supplementary movies 1–4 for $Bi = 0,\ 0.5,\ 2$ and 3, respectively.) The volume fraction ϕ time series and statistics are shown in figure 2(*a*) and (*b*,*c*), respectively. Here, ϕ increases with Bi non-trivially, with fluctuations of $\phi(t)$ (yielding and unyielding) in the statistically homogenous region $\bar{t}$ varying non-monotonically with Bi (figure 2*b*,*c*). At $Bi = 3$, the flow slowly transitions to a nearly completely jammed state, arresting the flow (as shown figure 2*a* and supplementary movie 4).

A notable feature of viscoelastic Kolmogorov flow is the formation of coherent structures (CS) of the stress field, the aforementioned arrowhead structures (Page *et al.* 2020), which are well-known for the purely viscoelastic case ($Bi = 0$) at $Wi > 10$ (Boffetta *et al.* 2005*b*; Berti *et al.* 2008; Berti & Boffetta 2010; Lewy & Kerswell 2025) and manifest as travelling elastic waves in the streamwise direction $t \gtrsim 300T$ (see $Bi = 0$ case in figure 1 and supplementary movie 1). For EVP cases, similar CS appear due to viscoelastic instabilities of high elasticity, where the addition of spatiotemporal interplay

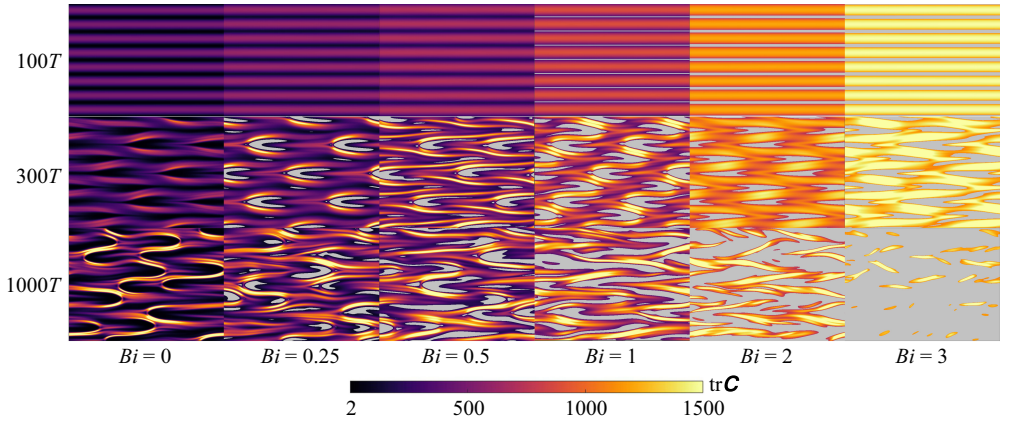

Figure 1. The EVP Kolmogorov flow in the ET regime. Representative snapshots of the polymer stretching tr $\boldsymbol{C}$ field $x = [0, 6 \times 2\pi)$ and $y = [0, 4 \times 2\pi)$ at various Bingham numbers, from $Bi = 0$ to 3 (columns), at different instances in time (rows): from the initial steady state $\sim 100T$ (top) to the transition $\sim 300T$ (middle), and the statistically homogenous regime $\bar{t} \gtrsim 600T$ (bottom). The grey areas represent the instantaneous unyielded $\mathcal{F} = 0$ regions. The first column $Bi = 0$ corresponds to a purely viscoelastic ET. Note, the colour bar is truncated below the true maximum at $\mathrm{tr}(\boldsymbol{C}) = 1500$ for visual clarity.

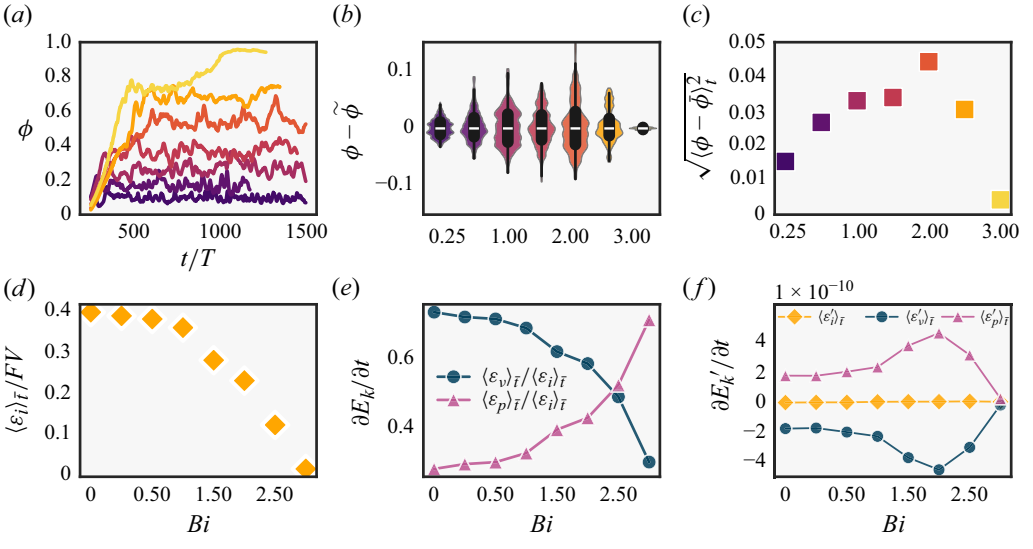

Figure 2. The solid (unyielded) volume fraction (*a*) time series $\phi(t)$ and its fluctuation statistics in the statistically homogeneous regime $\bar{t} \gtrsim 600T$, including (*b*) violin distribution density superimposed with box-whisker statistics relative to the median $\widetilde{\phi}$ (white line) and (*c*) the root-mean-squared fluctuations, where $\overline{\phi}$ is the temporal mean. The colour scheme in (*a*) refers to $Bi > 0$ as in (*b*) and (*c*). In (*b*), the box plots summarise the lower and upper quartile range of $\phi(t \geqslant \bar{t})$ with violins visualising the density and shape of the distribution. Notably, the strongest and broadest distribution of fluctuations in $\phi(t \geqslant \bar{t})$ is at $Bi = 2$. The system energy balance of the spatiotemporal mean for (*d*) instantaneous kinetic energy (3.1), (*e*) the viscous dissipation ϵ_v and elastic dissipation ϵ_p, and (*f*) their corresponding fluctuations (3.2). The directory including the data and the notebook that generated this figure can be accessed at https://www.cambridge.org/S0022112025104588/JFM-Notebooks/files/Figure_2/Fig2.ipynb.

between its viscoelastic-solid and-fluid behaviour leads to further dynamic structural stress deformations of the CS arrowheads (see supplementary movies). These modifications to the CS, which manifest even through the introduction of minimal plasticity at $Bi = 0.25$ (figure 1), immediately imply modifications to the modes of elastic waves, altering the transition route to the chaotic self-sustaining ET state (Kerswell & Page 2024; Lewy & Kerswell 2025). The spectral scaling exponent $E \propto k^{-\alpha}$ at $Bi = 0$ follows the exponent $\alpha = 4$ in agreement with Lellep, Linkmann & Morozov (2024), Lewy & Kerswell (2025) and all cases $Bi \leqslant 2.5$ are within the ET regime, as shown in supplemetary material, § S2, figure S3. Notably, increasing Bi progressively flattens the scaling exponent $4 > \alpha > 3$ and reduces the length of the inertial subrange. The unyielded (viscoelastic-solid) regions initially ($t \sim 100T$, top row in figure 1) form between shear layers (i.e. low-shear-rate regions) before manifesting behind the CS front $t \gtrsim 300T$. These low-shear regions effectively act as low-energy wells (Donley *et al.* 2023) that facilitate the formation of unyielded regions where, due to mass conservation, the stress is redistributed between shear layers (see the middle row $\sim 300T$ in figure 1). During the initial transition $\sim 300T$, the length of the unyielded regions in the CS increases with Bi due to a combination of greater ϕ (a consequence of increased yield criteria) and increased elastic effects with increasing Bi (at a given constant Wi), causing longer streaks. This behaviour is also apparent in the shape of unyielded regions as they become increasingly deformed and elongated. In the statistically homogeneous regime $\bar{t} \gtrsim 600T$ for $Bi = 0.25$ to 2.5, the unyielded regions manifest as local rearrangements with a broad distribution of sizes and shapes leading to further deformations of the CS (see figure 1 and figure 2*b–c*) – concomitant with the view that plastic events lead to a redistribution of elastic stresses in the system (Nicolas *et al.* 2018; N'Gouamba *et al.* 2019). For $Bi \geqslant 1$, unyielded regions interact across shear layers, merging or splitting each other, where increasing Bi increasingly disorganises the base flow until at the extreme $Bi = 3$ where the polymers are stretched in thin and highly localised regions. Notably, $Bi = 3$ is the only case with two distinct transitions at $\sim 300T$ and $\sim 800T$, reaching a statistically homogeneous regime $\bar{t} \gtrsim 1000T$ (figure 2*a*).

Increasing Bi decreases the overall energy (figure 2*d*), inferring a shift in the instantaneous kinetic energy balance $\partial E_k/\partial t \approx 0$ in the statistically homogeneous regime,

$$\frac{\partial E_k}{\partial t} = \langle \varepsilon_i \rangle_{\bar{t}} - \langle \varepsilon_v \rangle_{\bar{t}} - \langle \varepsilon_p \rangle_{\bar{t}} = 0, \quad t \geqslant \bar{t}, \tag{3.1}$$

where $\varepsilon_i = \langle \boldsymbol{u} \cdot \boldsymbol{F}_0 \rangle_{\boldsymbol{x}}$ is the energy input from the Kolmogorov forcing ($\boldsymbol{F}_0 = (F_0 \cos(y/\ell_y), 0)$), which is dissipated due to contributions from both the viscous Newtonian component $\varepsilon_v = 2\mu_s \langle \boldsymbol{D} : \boldsymbol{D} \rangle_{\boldsymbol{x}}$ and the non-Newtonian polymer component $\varepsilon_p = \langle \boldsymbol{u} \cdot (\nabla \cdot \boldsymbol{\sigma}) \rangle_{\boldsymbol{x}}$. Here, $\boldsymbol{D} = (1/2)(\nabla \boldsymbol{u} + \nabla \boldsymbol{u}^{\mathsf{T}})$ is the rate-of-strain tensor. The contributions of ε_p (elastic and plastic behaviour) increase with Bi and eventually dominate for $Bi \geqslant 2.5$, absorbing more energy than the dissipation of viscous kinetic energy (figure 2*e*). Fluctuations of the kinetic energy,

$$\frac{\partial E_k{}'}{\partial t} = \langle \varepsilon_i{}' \rangle_{\bar{t}} - \langle \varepsilon_v{}' \rangle_{\bar{t}} - \langle \varepsilon_p{}' \rangle_{\bar{t}} = 0, \quad t \geqslant \bar{t}, \tag{3.2}$$

in which the production term $\varepsilon_i{}' = \langle u_i{}' u_j{}' ((\partial \overline{u_i})/(\partial x_j)) \rangle_{\boldsymbol{x}} \approx 0$ (figure 2*f*) due to negligible inertial ($Re = 1$) contributions to the velocity fluctuations $\boldsymbol{u}' = \boldsymbol{u} - \bar{\boldsymbol{u}}$ (Gotoh & Yamada 1984; Boffetta *et al.* 2005*a*), where $\bar{\boldsymbol{u}} = \langle \boldsymbol{u} \rangle_{\bar{t}}$. Instead, the fluctuating non-Newtonian polymer term $\varepsilon_p{}' = 2\mu_s \langle \boldsymbol{D}' : \boldsymbol{D}' \rangle_{\boldsymbol{x}}$ is the positive source term to sustain

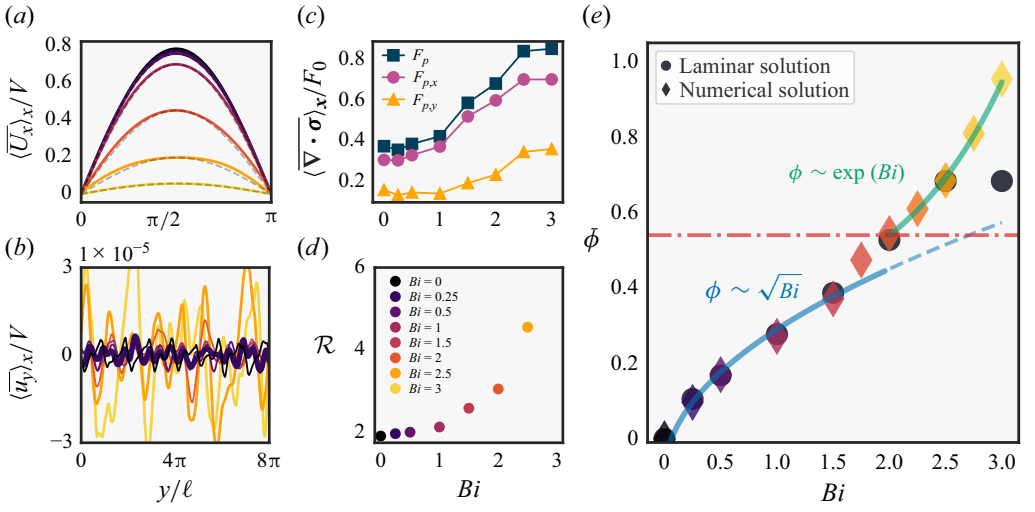

Figure 3. Features of jamming. Spatiotemporal mean of the velocity components: (*a*) the mean streamise flow profile $\langle \overline{U_x}(y^*)\rangle = (Kn_y)^{-1}\sum_{k=0}^{Kn_y-1}|\langle \overline{u_x}(y^*+k\pi)\rangle_x|$ along $y^* \in [0,\pi)$, (*b*) $\langle \overline{u_y}(y)\rangle_x$ and (*c*) the spatiotemporal mean of the polymer force $\langle \overline{\boldsymbol{\nabla}\cdot\boldsymbol{\sigma}}\rangle_{\boldsymbol{x}} = \langle \overline{\boldsymbol{F}_p}\rangle_{\boldsymbol{x}}$. In (*a*), velocity profiles are superimposed (grey dashed lines) with base sinusoidal profile scaled by the amplitude of each Bi case, i.e. $\max_y(\langle \overline{U_x}(y)\rangle)\cos(Ky)$. (*d*) Influence of plasticity on the energy injection rate per unit area, measured by flow resistance $\mathcal{R}$, the ratio between the power injected in the statistically homogeneous regime to the base laminar fixed point. (*e*) Volume fraction $\phi(t)$ as a function of Bingham number Bi, comparing (diamonds) the temporal mean $\bar{\phi} = \langle\phi\rangle_{\bar{t}}$ numerical simulations and (circles) the theoretically approximated ϕ (3.3). For $\phi < \phi_J$, we find that $\phi \sim \sqrt{Bi}$ (blue line) with the linear fit $\phi = 0.387\sqrt{Bi} - 9.7\times10^{-2}$ with a squared correlation coefficient $R^2 = 0.991$. Beyond the jamming transition $\phi_J \simeq 0.54$ at $Bi = 2$ (red dash-dot line) $\phi \sim \exp Bi$ (green line) with the linear fit $\phi = 3.2\times10^{-2}\exp Bi - 0.24$ with $R^2 = 0.999$. The directory including the data and the notebook that generated this figure can be accessed at https://www.cambridge.org/S0022112025104588/JFM-Notebooks/files/Figure_3/Fig3.ipynb.

and counteract the fluctuating viscous dissipation $\varepsilon_v{}' = \langle \boldsymbol{u}'\cdot(\boldsymbol{\nabla}\cdot\boldsymbol{\sigma}')\rangle_{\boldsymbol{x}}$, which vary non-monotonically with Bi (figure 2*f*). Interestingly, the viscous $\varepsilon_v{}'$ and elastic dissipation $\varepsilon_p{}'$ contributions to the energy budget clearly indicate a transition at $Bi = 2$, which aligns directly with the strongest and broadest distribution of fluctuations in $\phi(t)$ (figure 2*b* and *c*). Fluctuations in the dissipation then decrease for $Bi > 2$ (figure 2*f*) due to the polymer dissipation exceeding the viscous dissipation (figure 2*e*), i.e. the system becomes unable to sustain the flow due to strong fluctuations. The non-monotonic relationship between Bi and the fluctuations $\phi(t)$ along with the impaired flow energy for $Bi \geqslant 2$ are clear features of a typical phase transition – such a phase transition from a fluid-like to solid-like state is specifically known as jamming (Bonn *et al.* 2017).

A remarkable feature of the Kolmogorov flow is that even in the chaotic ET regime, the mean velocity (figure 3*a*) and conformation tensor are accurately described by sinusoidal profiles of the base flow with smaller amplitudes with respect to the laminar fixed point (Boffetta *et al.* 2005*a*,*b*; Berti & Boffetta 2010). We observe the $\langle \overline{U_x}\rangle$ profile for all Bi retain this feature (see figure S4 in the supplementary material) with the velocity front decreasing as Bi increases (figure 3*a*). Cases for $Bi \leqslant 0.5$ show traces of CS (figure 1) resembling purely elastic flow behaviour. The decreasing front velocity amplitude $\langle \overline{U_x}\rangle$ is minor for $Bi \leqslant 1$ but abruptly shifts for $Bi \geqslant 2$ decreasing dramatically, approaching static rest $\langle \overline{U_x}\rangle \to 0$ at $Bi = 3$ in figure 3*a* (see supplemetary movie 4). This infers a shift in the energy balance, in particular energy dissipation (figure 2*d–f*), further evident from the

increase in the transverse velocity component $\langle \overline{u_y}(y) \rangle_x$ and the polymer force $\boldsymbol{F}_p = \boldsymbol{\nabla} \cdot \boldsymbol{\sigma}$ with increasing Bi in figures 3(*b*) and 3(*c*), respectively. The deformation and locality of plastic events redistribute stresses anisotropically (Nicolas *et al.* 2018) as observed in figures 1 and 2, where the growth of these unyielded regions is strongly correlated with secondary flow effects (figures 3*b* and 3*c*), leading to a departure from the Kolmogorov base sinusoidal flow profile as Bi increases (figure 3*a*). Notably, the small transverse loads $F_{p,y}$ for $Bi > 1$ in figure 3(*c*) arise due to finite deformability (figure 1), which is a well-known feature of traditional jamming in dense suspension flows (see e.g. Cates *et al.* 1998).

We estimate the jamming transition for the present Kolmogorov flow configuration to be at the transition $Bi = 2$, $\phi_J \simeq 0.54$ (figure 3*e*), a value common in many traditional jammed systems, such as dense suspensions (Peters, Majumdar & Jaeger 2016; Bonn *et al.* 2017). Approaching the jamming transition from below $\phi \to \phi_J$ ($Bi < 2$), we find that $\phi \sim \sqrt{Bi}$ in figure 3(*e*). Above jamming $\phi \geqslant \phi_J$ is a clear deviation from $\phi \sim \sqrt{Bi}$, scaling as $\phi \sim \exp Bi$; such a dramatic change in behaviour further supports the features of phase transition observed in figure 2. To theoretically approximate ϕ in figure 3(*e*), we derive the laminar solution (see supplementary material, § S3),

$$\boldsymbol{C}_{lam}(y) = \begin{pmatrix} f^{-1}\left(1 + \dfrac{2K^2 Wi^2}{\mathcal{F}^2 f}\sin^2(Ky)\right) & K\dfrac{Wi}{\mathcal{F}f}\sin(Ky) \\ K\dfrac{Wi}{\mathcal{F}f}\sin(Ky) & 1 \end{pmatrix}. \tag{3.3}$$

Figure 3(*e*) shows the scaling behaviour, prior to and above ϕ_J, is in direct agreement with ϕ approximated by the laminar solution (3.3). The close agreement at intermediate $Bi \leqslant 2.5$ is surprising given the drastic flow deformations (figure 1). Interestingly, for $Bi = 3$, while (3.3) does not predict $\langle \phi \rangle_{\bar{t}}$ in $\bar{t} \gtrsim 1000T$ (figure 3*e*), it is consistent with $\langle \phi \rangle_t$ in the initial steady-state region $500T \lesssim t \lesssim 800T$ (figure 2*a*). Analogue scaling behaviour $\phi \sim \sqrt{Bi}$ for $\phi \leqslant \phi_J$ is commonly observed in traditional jamming transitions of dense suspensions (Peters *et al.* 2016; Bonn *et al.* 2017). Recent findings by Abdelgawad *et al.* (2023) showed that EVP fluids in inertial turbulence ($Re \gg 10^3$), with subdominant elastic effects $Wi \lesssim 1$, plasticity $Bi > 1$ increases intermittency. We find their results for $Bi > 1$ agree with our scaling $\phi \sim \sqrt{Bi}$ approaching the jamming transition (as shown in supplementary material, figure S5). Whether an analogue exponential scaling beyond the jamming transition $\phi > \phi_J$ is relevant in such inertia-dominated turbulent regimes remains to be observed.

The potential implications in practical applications of this elastic-plastic-induced jamming will be inferred by measuring the flow resistance to the power injected (Berti *et al.* 2008). The energy injection rate per unit area (power injected), $\mathcal{P}_{inj} = \langle \overline{\boldsymbol{u} \cdot \boldsymbol{F}} \rangle_{\boldsymbol{x}}$, with $\boldsymbol{F} = \boldsymbol{F}_0 + \boldsymbol{F}_p$. In the laminar steady state, denoted by $\widehat{\cdot}$, $\partial_x \widehat{P}$ is constant and $\langle u_x \rangle_{\boldsymbol{x}} \approx \widehat{u}$, where $\widehat{\mathcal{P}_{inj}} = (1/2) V F_0$ (see supplemetary material, § S3.1). Due to the body force and the energy dissipated by the elastic-plastic-viscous effects, the flow resistance, $\mathcal{R} = \mathcal{P}_{inj}/\widehat{\mathcal{P}_{inj}} = \langle \overline{\boldsymbol{u} \cdot \boldsymbol{F}} \rangle_{\boldsymbol{x}}/(1/2 V F_0)$, gradually increases for $Bi \leqslant 1$ before shifting as a consequence of the jamming phase change (figure 3*d*). Moreover, our jamming transition scaling behaviour $\phi \sim \sqrt{Bi}$ has a potentially direct connection with other known scaling, namely, the Fanning friction factor in channel flows (Rosti *et al.* 2018) and the pressure drop in porous media flows (De Vita *et al.* 2018).

The macroscopic point of view of jamming in EVP materials is typically considered as the yield criteria, an immediate shift to a flow state once a certain stress threshold is reached, e.g. if the flow applied induces sufficiently high shear (Dennin 2008;

Bonn *et al.* 2017). We demonstrate the statistically homogenous dynamics of EVP Kolmogorov flows in the ET regime (dominant elastic instabilities) across a range of Bi (ϕ) align with the laminar scaling prediction below and above the transition ϕ_J, i.e. $\phi \sim \sqrt{Bi}$ and $\phi \sim \exp Bi$, respectively (figure 3*e*). The connection to jamming in this work has profound implications on EVP fluid flows; it describes plastic events, such as plastic 'plugs' in channel flows (Rosti *et al.* 2018; Izbassarov *et al.* 2021; Villalba *et al.* 2023), as a phase-change phenomenon, whose consequences in dynamic behaviour are analogous to traditional jamming but different in the sense that it is induced by dynamic structural stress deformations arising from viscoelastic flow instabilities. This dependency on the locality of these plastic-induced stress deformations is all important as these depend on the local geometry and flow field, implying that the nature of this jamming transition $\phi \to \phi_J$ varies from one configuration to another. For example, for the square-root scaling in the form $\phi \sim c_1\sqrt{Bi} + c_2$ (see e.g. figure 3), the constants c_1 and c_2 depend on the flow configuration, Wi, and Re. Similarly, the exponential scaling $\phi \sim \exp Bi$ may also be influenced by such factors, and its precise form could vary across flow configurations. In support of this, our previous work (Dzanic *et al.* 2024) found that two extensional flow benchmark problems, with the same dimensionless variables and similar flow-type distribution, result in very different dynamic responses to plasticity with different ϕ across a range of Bi. The consequence of this dependency, for example, is that the bulk shear rheology characterisation of the material (Cheddadi, Saramito & Graner 2012; Varchanis *et al.* 2020) – commonly performed in Couette-type geometries – will be subject to jamming dynamics different from those experienced in the actual flow configuration of the application, making their performance in practice unpredictable. Such issues in translating rheological characterisation to quantify flow performance in actual flow configurations have recently been reported as major challenges in predicting the flow performance of functional EVP materials (Bertsch *et al.* 2022). Predicting and controlling jamming is crucial in, e.g. 3-D extrusion biomaterial printing, where the jamming of soft materials during extrusion has a negative impact on both the print quality and cell viability (Xin *et al.* 2021).

4. Discussion

We have studied inertialess instabilities of EVP fluid flows in the ET regime and discovered these to transition towards jamming, featuring rich dynamics with a delicate balance between solid-like and liquid-like behaviour. We show that in the formation of spatiotemporal arrowhead structures, highly localised polymer stress regions act as local low-stress energy wells, facilitating the formation of unyielded solid regions. These localised unyielded structures, in turn, deform and redistribute stresses anisotropically, leading to an interplay between viscoelastic and plastic behaviour, which dominates and absorbs more energy than viscous dissipation. Consequently, increasing plastic effects leads to jamming transition, sharing features directly analogous to traditional jamming of dense suspensions characterised by a drastic change in flow behaviour that is slow, minimally diffusive and rigid-like with finite deformability leading to transverse loads. In particular, we find the volume fraction scales as $\phi \sim \sqrt{Bi}$ until the 'jamming' phase transition $\phi_J \simeq 0.54$ where the behaviour changes dramatically, scaling as $\phi \sim \exp Bi$. Viscoelastic Kolmogorov flow in 2-D has recently been shown to differ from 3-D (Lellep *et al.* 2024), suggesting limited experimental realisability of the plasticity-induced modifications to the arrowhead structures in our simulations due to 3-D dependencies. Nevertheless, key findings in this work are that shear-dependent problems in the ET regime reach a jammed state with increasing Bi, scaling as $\phi \sim \sqrt{Bi}$ and $\phi \sim \exp Bi$ beyond

the jamming transitions. Moreover, we demonstrated our $\phi \sim \sqrt{Bi}$ scaling to hold for inertia-dominated turbulent flows by Abdelgawad *et al.* (2023) (supplementary material, figure S5) and, as such, suspect our findings to hold in shear flows where elasticity and inertia are dominant, i.e. within the elasto-inertial turbulence regime. The exact interactions between the flow and elastic scales with the plastic events remain unclear, and more work is required to understand the effect of elasticity Wi on the scaling behaviour beyond the jamming transition $\phi > \phi_J$. In particular, a rigorous understanding of the $\phi \sim \exp Bi$ scaling may benefit from asymptotic analysis or dimensionless modelling in the limit of large Bi.

The complex intermittent nature of inertialess EVP fluid flows makes their applications unpredictable and difficult to control, such as with the formation of plugs leading to increased flow resistance in practice. Indeed, previous works on EVP fluid flows describe the increase in volume fraction as a general effect of increasing the Bingham number Bi. However, no previous work has connected this phenomenon to jamming – this connection crucially reclassifies it as a phase-change phenomenon – and the analogous features which describe the impact of this transition. The dependence of plasticity-induced stress deformations on local conditions implies that the jamming behaviour observed in one configuration may differ significantly in another. Consequently, bulk shear rheology measurements may fail to predict the jamming dynamics and flow performance of EVP materials in more application-relevant configurations – ranging from industrial food, cosmetic and mining processes (e.g. moulding, extrusion, silo clogging, etc.) to emerging technologies (e.g. printing biomaterials), where unexpected jamming can lead to extreme events, disrupt performance or lead to critical failures.

Supplementary material and movies. Supplementary material, movies and Computational Notebook files are available at https://doi.org/10.1017/jfm.2025.10458. Computational Notebooks can also be found online at https://www.cambridge.org/S0022112025104588/JFM-Notebooks.

Acknowledgements. The authors acknowledge the assistance given by Research IT and the use of the Computational Shared Facility at The University of Manchester, and the High-Performance Computing facilities at Queensland University of Technology. The authors thank the anonymous reviewers whose feedback contributed to the overall improvement of the final manuscript.

Funding. E.S. is supported by the Australian Research Council (ARC- FT200100446).

Declaration of interests. The authors report no conflict of interest.

Data availability statement. The data that support the findings of this study are openly available in the JFM Notebook, reproducing figures 2 and 3.

References

Abdelgawad, M., Cannon, I. & Rosti, M. 2023 Scaling and intermittency in turbulent flows of elastoviscoplastic fluids. *Nat. Phys.* **19**, 1–5.

Balmforth, N.J., Frigaard, I.A. & Ovarlez, G. 2014 Yielding to stress: recent developments in viscoplastic fluid mechanics. *Annu. Rev. Fluid Mech.* **46**, 121–146.

Berti, S., Bistagnino, A., Boffetta, G., Celani, A. & Musacchio, S. 2008 Two-dimensional elastic turbulence. *Phys. Rev. E* **77**, 055306.

Berti, S. & Boffetta, G. 2010 Elastic waves and transition to elastic turbulence in a two-dimensional viscoelastic Kolmogorov flow. *Phys. Rev. E* **82**, 036314.

Bertsch, P., Diba, M., Mooney, D.J. & Leeuwenburgh, S.C.G. 2022 Self-healing injectable hydrogels for tissue regeneration. *Chem. Rev.* **123** (2), 834–873.

Boffetta, G., Celani, A. & Mazzino, A. 2005*a* Drag reduction in the turbulent Kolmogorov flow. *Phys. Rev. E* **71**, 036307.

Boffetta, G., Celani, A., Mazzino, A., Puliafito, A. & Vergassola, M. 2005*b* The viscoelastic Kolmogorov flow: eddy viscosity and linear stability. *J. Fluid Mech.* **523**, 161–170.

BONN, D., DENN, M.M., BERTHIER, L., DIVOUX, T. & MANNEVILLE, S. 2017 Yield stress materials in soft condensed matter. *Rev. Mod. Phys.* **89**, 035005.
CATES, M.E., WITTMER, J.P., BOUCHAUD, J.-P. & CLAUDIN, P. 1998 Jamming, force chains, and fragile matter. *Phys. Rev. Lett.* **81**, 1841–1844.
CHEDDADI, I., SARAMITO, P. & GRANER, F. 2012 Steady Couette flows of elastoviscoplastic fluids are nonunique. *J. Rheol.* **56** (1), 213–239.
COCHRAN, J.O., CALLAGHAN, G.L., CAVEN, M.J.G. & FIELDING, S.M. 2024 Slow fatigue and highly delayed yielding via shear banding in oscillatory shear. *Phys. Rev. Lett.* **132**, 168202.
COUCHMAN, M.M.P., BENEITEZ, M., PAGE, J. & KERSWELL, R.R. 2024 Inertial enhancement of the polymer diffusive instability. *J. Fluid Mech.* **981**, A2.
DATTA, S.S. *et al.* 2022 Perspectives on viscoelastic flow instabilities and elastic turbulence. *Phys. Rev. Fluids* **7**, 080701.
DE VITA, F., ROSTI, M.E., IZBASSAROV, D., DUFFO, L., TAMMISOLA, O., HORMOZI, S. & BRANDT, L. 2018 Elastoviscoplastic flows in porous media. *J. Non-Newtonian Fluid Mech.* **258**, 10–21.
DENNIN, M. 2008 Discontinuous jamming transitions in soft materials: coexistence of flowing and jammed states. *J. Phys.: Condens. Matt.* **20** (28), 283103.
DONLEY, G.J., NARAYANAN, S., WADE, M.A., PARK, J.D., LEHENY, R.L., HARDEN, J.L. & ROGERS, S.A. 2023 Investigation of the yielding transition in concentrated colloidal systems via rheo-XPCS. *Proc. Natl Acad. Sci. USA* **120** (18), e2215517120.
DUBIEF, Y., TERRAPON, V.E. & HOF, B. 2023 Elasto-inertial turbulence. *Annu. Rev. Fluid Mech.* **55** (2023), 675–705.
DZANIC, V., FROM, C.S. & SAURET, E. 2022*a* Assessment of polymer feedback coupling approaches in simulation of viscoelastic fluids using the lattice Boltzmann method. *Comput. Fluids* **246**, 105629.
DZANIC, V., FROM, C.S. & SAURET, E. 2022*b* Conserving elastic turbulence numerically using artificial diffusivity. *Phys. Rev. E* **106**, L013101.
DZANIC, V., FROM, C.S. & SAURET, E. 2022*c* The effect of periodicity in the elastic turbulence regime. *J. Fluid Mech.* **937**, A31.
DZANIC, V., FROM, C.S. & SAURET, E. 2022*d* A hybrid lattice Boltzmann model for simulating viscoelastic instabilities. *Comput. Fluids* **235**, 105280.
DZANIC, V., FROM, C.S. & SAURET, E. 2024 Influence of plasticity on inertialess viscoelastic instabilities in elongational flow regimes. *Phys. Rev. Fluids* **9**, 063301.
GOTOH, K. & YAMADA, M. 1984 Instability of a cellular flow. *J. Phys. Soc. Japan* **53**, 3395–3398.
GROISMAN, A. & STEINBERG, V. 2000 Elastic turbulence in polymer solution flow. *Nature* **405**, 53–55.
GUPTA, A. & VINCENZI, D. 2019 Effect of polymer-stress diffusion in the numerical simulation of elastic turbulence. *J. Fluid Mech.* **870**, 405–418.
IZBASSAROV, D., ROSTI, M.E., BRANDT, L. & TAMMISOLA, O. 2021 Effect of finite Weissenberg number on turbulent channel flows of an elastoviscoplastic fluid. *J. Fluid Mech.* **927**, A45.
JEROLMACK, D.J. & DANIELS, K.E. 2019 Viewing Earth's surface as a soft-matter landscape. *Nat. Rev. Phys.* **1**, 716–730.
KERSWELL, R.R. & PAGE, J. 2024 Asymptotics of the centre-mode instability in viscoelastic channel flow: with and without inertia. *J. Fluid Mech.* **991**, A13.
LELLEP, M., LINKMANN, M. & MOROZOV, A. 2024 Purely elastic turbulence in pressure-driven channel flows. *Proc. Natl Acad. Sci. USA* **121** (9).
LEWY, T. & KERSWELL, R.R. 2025 Revisiting two-dimensional viscoelastic Kolmogorov flow: a centre-mode-driven transition. *J. Fluid Mech.* **1007**, A55.
MOROZOV, A. 2022 Coherent structures in plane channel flow of dilute polymer solutions with vanishing inertia. *Phys. Rev. Lett.* **129**, 017801.
N'GOUAMBA, E., GOYON, J. & COUSSOT, P. 2019 Elastoplastic behavior of yield stress fluids. *Phys. Rev. Fluids* **4**, 123301.
NICHOLS, J., GUY, R.D. & THOMASES, B. 2025 Period-doubling route to chaos in viscoelastic Kolmogorov flow. *Phys. Rev. Fluids* **10**, L041301.
NICOLAS, A., FERRERO, E.E., MARTENS, K. & BARRAT, J.-L. 2018 Deformation and flow of amorphous solids: insights from elastoplastic models. *Rev. Mod. Phys.* **90**, 045006.
PAGE, J., DUBIEF, Y. & KERSWELL, R.R. 2020 Exact traveling wave solutions in viscoelastic channel flow. *Phys. Rev. Lett.* **125**, 154501.
PETERLIN, A. 1961 Streaming birefringence of soft linear macromolecules with finite chain length. *Polymer* **2**, 257–264.
PETERS, I.R., MAJUMDAR, S. & JAEGER, H.M. 2016 Direct observation of dynamic shear jamming in dense suspensions. *Nature* **532**, 214–217.

PETRIE, C.J.S. & DENN, M.M. 1976 Instabilities in polymer processing. *AIChE J.* **22** (2), 209–236.
ROSTI, M.E., IZBASSAROV, D., TAMMISOLA, O., HORMOZI, S. & BRANDT, L. 2018 Turbulent channel flow of an elastoviscoplastic fluid. *J. Fluid Mech.* **853**, 488–514.
SARAMITO, P. 2007 A new constitutive equation for elastoviscoplastic fluid flows. *J. Non-Newtonian Fluid Mech.* **145**, 1–14.
SMITH, B.T. & HASHMI, S.M. 2024 In situ polymer gelation in confined flow controls intermittent dynamics. *Soft Matt.* **20** (8), 1858–1868.
STEINBERG, V. 2021 Elastic turbulence: an experimental view on inertialess random flow. *Annu. Rev. Fluid Mech.* **53** (1), 27–58.
VARCHANIS, S., HAWARD, S.J., HOPKINS, C.C., SYRAKOS, A., SHEN, A.Q., DIMAKOPOULOS, Y. & TSAMOPOULOS, J. 2020 Transition between solid and liquid state of yield-stress fluids under purely extensional deformations. *Proc. Natl Acad. Sci. USA* **117**, 12611–12617.
VILLALBA, M.E., DANESHI, M., CHAPARIAN, E. & MARTINEZ, D.M. 2023 Atypical plug formation in internal elastoviscoplastic fluid flows over non-smooth topologies. *J. Non-Newtonian Fluid Mech.* **319**, 105078.
XIN, S., DEO, K.A., DAI, J., PANDIAN, N.K.R., CHIMENE, D., MOEBIUS, R.M., JAIN, A., HAN, A., GAHARWAR, A.K. & ALGE, D.L. 2021 Generalizing hydrogel microparticles into a new class of bioinks for extrusion bioprinting. *Sci. Adv.* **7** (42), eabk3087.
YERASI, S.R., PICARDO, J.R., GUPTA, A. & VINCENZI, D. 2024 Preserving large-scale features in simulations of elastic turbulence. *J. Fluid Mech.* **1000**, A37.
ZHANG, Y.S., DOLATSHAHI-PIROUZ, A. & ORIVE, G. 2024 Regenerative cell therapy with 3D bioprinting. *Science* **385**, 604–606.